ARTICLE OPEN

Highly transparent conductors for optical and microwave access to spin-based quantum systems

Robert Staacke [1]*, Roger John[1], Max Kneiß [2], Marius Grundmann[2] and Jan Meijer[1]

Spin-based quantum systems are among the best sensors in terms of sensitivity and spatial resolution for a variety of physical properties. A key factor to broaden the range of applications is the control over the microwave field used to manipulate the quantum system. We present the implementation of a transparent microwave conductor, suitable for optical read-out of a spin-based quantum sensor. For this, the interaction of an indium tin oxide (ITO) strip line on diamond with nitrogen vacancy centres was investigated. The amorphous ITO can be fabricated at room temperature, has a transmittance larger than 80% in the visible spectrum and a low resistivity. We show that these strip lines are completely scalable which enables highly homogeneous microwave fields from the nanometre up to the millimetre scale. ITO structures can therefore serve as excellent transparent microwave conductors, widening the current use of spin-based quantum sensors.

npj Quantum Information (2019)5:98 ; https://doi.org/10.1038/s41534-019-0216-1

INTRODUCTION

Apart from being an atom-sized sensor for magnetic fields,[1] electric fields,[2] pressure,[3] and temperature,[4] the nitrogen vacancy centre (NV) in diamond is a promising candidate for qubits in quantum computers.[5] Most sensing techniques utilizing NVs require a defined microwave field near the centres, e.g. optically (ODMR) or photo-electrically (PDMR) detected magnetic resonance.[6,7] For these applications, the microwave field is typically realised by using simple gold or copper wires near the diamond surface. To manipulate the NV spin, an oscillating magnetic field in the GHz region is needed. Large structures are used to optimise the microwave power distribution over the device, since the magnetic field strength of a wire decreases with $1/r$ with respect to the wire. Here, r is the distance to the centre of the wire. A simple structure often applied is an omega (Ω) shaped conductor fabricated on the diamond surface.[8,9] A disadvantage of this technique is that, for small structures, a considerably large area of the sensor would be blocked. These structures are also difficult to combine with PDMR, since a crossing of conductors needs to be avoided. Additionally, there are approaches for even larger but more homogeneous antenna structures in the range of millimetres but these have the disadvantage of a low bandwidth.[10,11] For minimising the sensor size without blocking the excitation or fluorescence, transparent conducting thin films are promising materials as microwave conductors. Optically transparent electronics already have many applications such as solar cells,[12] photo detectors,[13] transistors,[14] diodes[15] or as conductive films in microscopy.[16] The most common materials used as transparent conductors are zinc-oxide (ZnO) and indium-tin-oxide (ITO). It was shown that ZnO as a dielectric material is well suited to produce surface acoustic waves on diamond in the GHz region.[17] For highly conductive ZnO thin films, temperatures up to 400 °C are required,[18] which can be disadvantageous for heat sensitive applications. The film quality also depends critically on the diamond substrate orientation where (100) and (110) planes typically result in lower quality films compared to (111) planes.[19] Additionally, ZnO crystallises rapidly during the creation process

which is why it is difficult to produce amorphous films.[20] ITO is the ideal candidate to compensate for these downsides. It is possible to produce amorphous ITO thin films at room temperature by pulsed laser deposition, while having optical and electrical properties similar to ZnO.[21]

In this work, we present the use of transparent conductors in combination with NV centres in diamond enabling the fabrication of completely transparent devices. It is possible to determine the oscillating magnetic field strength of a microwave conductor by measuring the Rabi frequency[22,23] of a single NV centre. This principle is used to determine the distribution of the strength of the microwave field of an ITO strip line. The ITO strip line was created by electron lithography and pulsed laser deposition on a (001) diamond plane along the [1$\bar{1}$0] direction. By choosing NVs with [111] and [$\bar{1}\bar{1}$1] orientation and different distances to the centre of the strip line, we could measure the projection of the magnetic field perpendicular to the NV directions. We show by simulating the dominant field mode of the structure and comparing the results with our measurements, that it is possible to predict the magnetic field vector around the strip line.

RESULTS

The 300 nm thick and 20 μm wide ITO strip line on diamond used in this work is shown in Fig. 1a. A layer of single NVs was created by the implantation of CN^- molecules with 100 keV. According to SRIM simulations,[24] 90% of the implanted NVs are located in the range of (67 ± 16) nm below the diamond surface. A laser scanning confocal microscope image of the strip line is shown in Fig. 1b. Single NVs can be observed over the whole area especially through the ITO but with increased background. The intense parts of the strip line edges are areas with an increased thickness of the ITO which are a result of the lithography process.

To verify the transmittance of the ITO layer, fluorescence spectra of single NVs through the strip line were compared to single NVs without ITO on top. The measured spectra were background-corrected by subtracting the spectra of the

¹Applied Quantum Systems, Felix Bloch Institute Leipzig University, Leipzig, Saxony, Germany. ²Semiconductor Physics Group, Felix Bloch Institute Leipzig University, Linnéstraße 5, Leipzig, Germany. *email: robert.staacke@physik.uni-leipzig.de
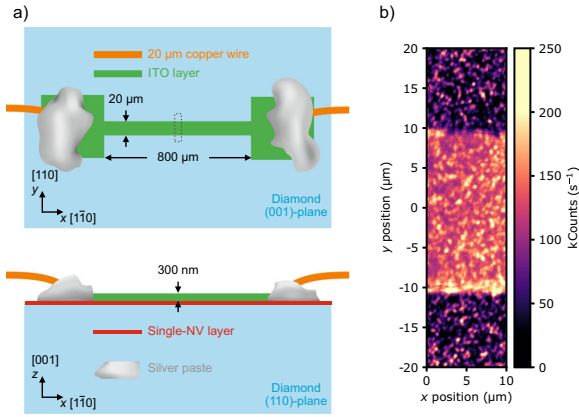
Fig. 1 **a** Top and side view of the ITO structure. The dashed box marks the confocal scanning area. **b** Laser scanning confocal microscope image of the diamond with the ITO strip line. Emission of single NV centres can be observed over the whole area. The 20 μm wide ITO strip line is clearly visible as a region with increased background fluorescence

fluorescence next to the centre. The fluorescence of the ITO was measured by subtracting the diamond background from a spectrum of the ITO strip line with no NVs below. All NV spectra were obtained at laser powers much larger than their saturation power. This ensures that the fluorescence strength of the NVs with or without ITO on top is the same. Typical spectra of our sample are shown in Fig. 2a. All three spectra are normalised by the peak value of the background-corrected spectra of a single NV without ITO on top. The transmittance of the ITO layer of 84(6)% in the range of 620 nm–850 nm was obtained by a linear fit with the spectra of a single NV without ITO on top. In the same wavelength range, the background fluorescence produced by the ITO is twice as intense as of a single NV. The reduced transmittance of the ITO layer is not caused by the absorption in the ITO layer or the reduced reflection between the diamond-ITO and ITO-air interfaces compared to a bare diamond-air interface. We believe that the high dispersion of the ITO is the cause for the reduced fluorescence of the NVs below the ITO (see Supplementary Note 1).

Van der Pauw measurements[25] were done on a circular 1 mm diameter ITO layer deposited on a (100) optical grade diamond from Element Six Technologies.[26] The resistivity $\rho_{ITO} = 2.525(5) \times 10^{-6}$ Ωm, carrier concentration $n_{ITO} = 9(6) \times 10^{20}$ cm^{-3} and electron mobility $\mu_{ITO} = 27(10)$ cm^2(Vs)$^{-1}$ of the ITO layer were measured, which are comparable to literature values.[27,28] These electrical parameters served as input for a 2D Comsol mode analysis[29] to simulate the magnetic field distribution **B** in the depth of the implanted NVs. The spin of the NV centre can only be rotated by fields perpendicular to its axis. Projecting the magnetic field vector **B** of the microwave perpendicular to the NV directions ([111] and [$\bar{1}\bar{1}1$]) gives a scalable function (see Supplementary Note 2):

$$|\mathbf{B}_\perp(y)| = a \cdot \left| \sqrt{\frac{2}{3}} B_z(y-b) \mp \frac{1}{\sqrt{3}} \cdot B_y(y-b) \right|, \quad (1)$$

with scaling parameter a and shift b. The parameter a scales the function since the mode analysis only gives a relative field distribution and not the absolute amplitudes. The parameter b shifts the function in the y direction and compensates for the coordinate system mismatch between the measurement and the simulation. The Rabi frequency ω_{rabi} is given by:

$$\omega_{rabi} = \gamma \cdot |\mathbf{B}_\perp|. \quad (2)$$

The electron gyromagnetic ratio γ is ~28 MHz/mT. $\mathbf{B}_\perp$ is the projection of the microwave magnetic field on the plane perpendicular to the NV direction. We measured the Rabi frequency for both directions at an externally applied static magnetic field of 70 mT with 30 dBm input power (see Supplementary Note 3 for power dependency) and used Eq. (1, 2) to determine the scaling and shift parameter. The measured data and the fit curves with standard errors are shown in Fig. 2b. The shift error is about 3% and the scaling factor error is 5%. Using the scaling factor from the fits, the two-dimensional distribution of the magnetic field vector $\mathbf{B}(y, z)$ can be calculated from the mode simulations. Figure 3 shows the absolute value of the magnetic field $|\mathbf{B}(y, z)|$ and the projections in different directions in the cross-sectional area below the strip line.

DISCUSSION

Our simulations are in an excellent agreement with the measured Rabi frequencies of two different NV orientations. Also, the strip line structure has no negative influence on the T_2 times or the signal to noise ratio in optically detected paramagnetic resonance (ODMR) experiments of the NVs below the ITO (see Supplementary Note 4). This enables us to study the projections of the microwave field in other directions. The projection perpendicular to the [001] direction shown in Fig. 3b shows a strong local confinement of the field below the strip line. Since the strip line is much thinner than its width W, we can approximate the structure with a 2D conductor. For distances much smaller than the wavelength, the Biot-Savart law gives the magnetic field perpendicular to the [001] direction (y direction) $\mathbf{B}_y^{(2D)}$ (see Supplementary Note 5):

$$\mathbf{B}_y^{(2D)}(y=0) = -\frac{\mu_0}{2\pi} \frac{I}{W} \cdot \arctan\left(\frac{W}{2z}\right) \quad (3)$$

$$\mathbf{B}_y^{(2D)}\left(z \ll \left|y \pm \frac{W}{2}\right|\right) \approx \begin{cases} \frac{\mu_0}{4\pi} \frac{I}{W}\left(\frac{2z}{2y-W} - \frac{2z}{2y+W}\right) & |y| > \frac{W}{2} \\ \frac{\mu_0}{4\pi} \frac{I}{W}\left(\pi + \frac{2z}{2y-W} - \frac{2z}{2y+W}\right) & |y| < \frac{W}{2} \end{cases} \quad (4)$$

In Fig. 4a, the y component of $\mathbf{B}^{(2D)}$ right below the strip line is shown. The analytic solution matches our Comsol simulations perfectly with a standard error in z direction of 10^{-4}, verifying the applicability of the simple 2D model. This means the strip line can be considered as a conductor of infinite length and finite width with a homogeneous current density. Below the strip line, the field is homogeneous, while beyond the strip line the field follows a r^{-1} dependency, with the pole on the edge of the line. In z direction, the decay follows $\arctan(r^{-1})$ which exhibits a significantly less rapid decrease than the r^{-1} function in the near field. For a distance of half the width of the strip line, the field strength decays only by a factor of 2. If used on [111] oriented NVs in a (111) diamond, this behaviour of the near field can be used to selectively address only NV centres below the strip line. Fortunately, on a (111) diamond, it is possible to create NVs with more than 94% alignment in the [111] direction,[30,31] which simplifies the device fabrication. This enables low microwave power operation, since the distance to the strip line is much smaller and constant in contrast to typical microwave conductors such as copper or gold wires. For nano sensing applications, where distances between the NV centres and the object need to be of a few nanometres, the ITO strip line can be used on the backside of a thin diamond plate. The magnetic field distribution in z direction can be stretched to reach deeper in the diamond by adjusting the width of the strip line (see Supplementary Note 5). This enables experiments where an optical access is not possible from the sensing side and the diamond surface must be free from microwave structures. The scalability of ITO strip lines is demonstrated by an exemplary simulation of a 300 nm thick
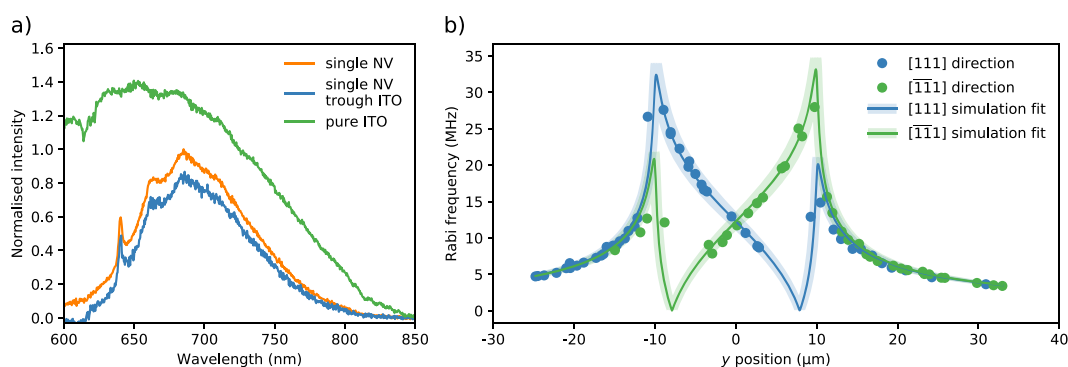
Fig. 2 **a** Background-corrected spectra of pure ITO (green line) and a single NV through the ITO strip line (blue line) and without ITO on top (orange line). The intensity of each spectra is normalised by the peak value of the spectra of a single NV without ITO on top. **b** Measured Rabi frequencies of single NVs with different distances to the strip line. Each point represents a single NV in [111] (blue) or [$\bar{1}11$] (green) direction. The solid lines are Comsol simulation fits with Eqs. (1, 2) and the shaded areas represent the standard deviation error of the fit parameters a and b. The centre of the strip line is located at a y position of 0 μm
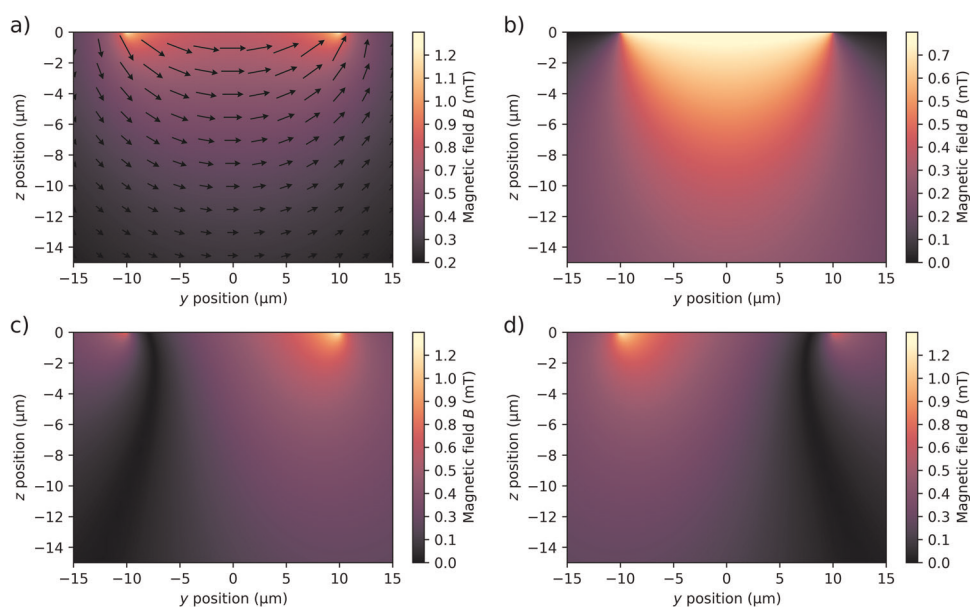
Fig. 3 **a** Simulation of the absolute value of the magnetic field of the microwave with field direction indicated as arrows. The field strength was scaled with the fit parameters given in Eq. (1). The projections of the field perpendicular to the **b** [001] direction, **c** [$\bar{1}11$] direction and **d** [111] direction are shown. Negative z position values are located inside the diamond. The strip line is located between −10 μm and 10 μm in y direction and from 0 to 300 nm in z

and 500 μm wide ITO strip line. In Fig. 4b, the normalised results of the simulation of the magnetic field projection perpendicular to the [001] direction at a depth of 67 nm are shown. From the inset, it can be seen that the field strength varies less than 0.4% over a range of 400 μm. In combination with a (111) diamond, this enables extremely large devices with homogeneous microwave fields over the whole diamond. But also structures with nanometre scale are possible, e.g., for selective addressing of spins or small sensors. Since ITO is transparent for wavelengths larger than ≈ 400 nm and biocompatible,[32–36] such devices could be used to simultaneously perform fluorescence microscopy and sensing (e.g. magnetometry, temperature sensing) with NV centres. This would allow a whole new area of applications in biology or medicine, since it would be possible to simultaneously measure fluorescence markers and perform measurements of physical properties with NV centres.

METHODS

Sample preparation

For the single NV measurements, a conventional electronic grade (B < 1 ppb, N < 5 ppb) chemical vapour depositon (CVD) diamond (Element Six Technologies[26]) was used. The substrate used for the electrical character-isation was an optical grade (N ≈ 1ppb) CVD diamond (Element Six Technologies[26]). For the creation of single NV centres, CN-molecules were implanted with an energy of 100 keV and a dose of 10^{10} cm^{-2}. The diamond was annealed at 900 °C for 4 h in vacuum and cleaned in a boiling mixture of nitric acid (100%), sulfuric acid (100%) and perchloric acid (70%) with a mixing ratio of 1:3:1 for 4 h. Electron beam lithography was performed by using a positive resist (Polymethylmethacrylat (PMMA), AR-P 671.05 from Allresist GmbH, thickness ≈1 μm) with ≈10 nm conducting resist (Electra 92 from Allresist GmbH) to minimize charge drifts. The applied PMMA was baked at 180 °C for 20 min. For the Electra 92 resist no further baking step was used, since a additional baking step causes the PMMA to form cracks. The electron dose used for the lithography was 500 μC(cm)$^{-2}$. The ITO layers were grown by pulsed laser
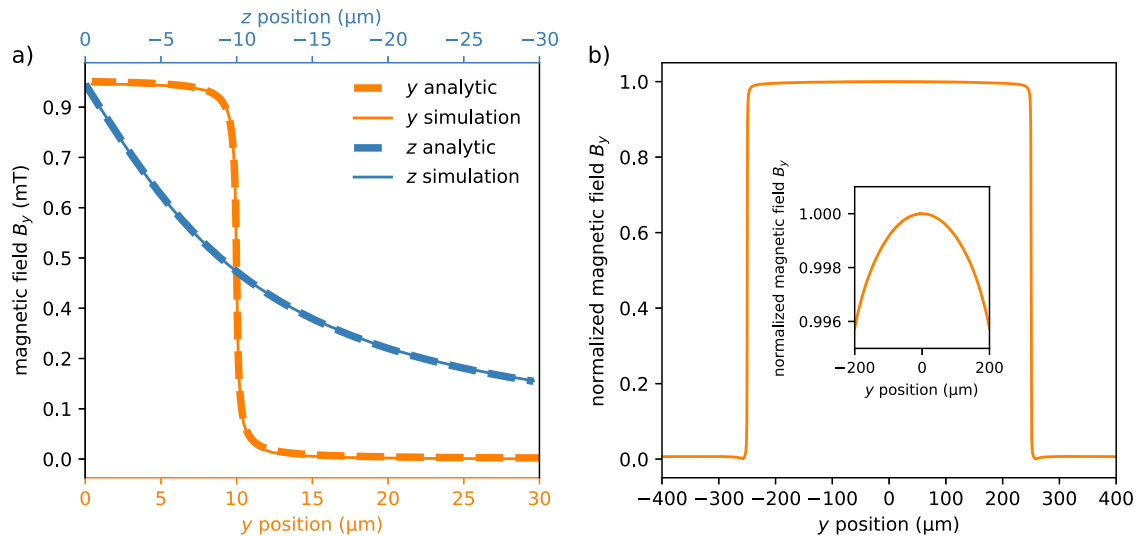
Fig. 4 a Simulation and analytic calculation of the y component of the magnetic field in dependence on the distance to the centre of the strip line in y and z direction for the ITO strip line measured in this work. The origin is in the middle of the strip line on the diamond surface. The Comsol simulations were fitted with the analytic solutions of $\mathbf{B}_y^{(2D)}$. **b** Exemplary simulation to demonstrate the scalability of the strip line structure. The normalised results from the simulation of the magnetic field perpendicular to the [001] direction of a 500 µm wide strip line are shown. All other input parameters are the same as for the strip line produced for this work. In the inset the homogeneous part of the B_y field below the strip line is enlarged

deposition employing a 248 nm KrF excimer laser (Coherent LPX Pro 305 F). The laser fluence was adjusted to ~2 Jcm^{-2} incident on the target surface. The repetition rate of 10 Hz was chosen to apply a total of 10,000 pulses. The used ceramic target consisted of In_2O_3 and 1 wt.% SnO_2. This is equal to a cation ratio Sn/(In+Sn) of 0.92 at.%. The In_2O_3 (purity 99.994%, Alfa Aesar) and SnO_2 (purity 99.9%, Alfa Aesar) powders were ball-milled, homogenized, cold-pressed and subsequently sintered in air at 1600 °C for 48 h. The oxygen partial pressure during deposition was set to 0.01 mbar, while the substrate was kept at room temperature to ensure amorphous growth of the ITO layer. These parameters resulted in a growth rate of 30 pm/pulse. The composition of the resulting ITO layer was checked with energy dispersive X-ray analysis (EDX). A tin content of 0.58(13) wt.% was found, which corresponds to a cation ratio Sn/(In+Sn) of 0.7(3) at.%. Superconducting quantum interference device (SQUID) measurements were performed on the ITO layers and no ferromagnetic signal could be detected in our amorphous thin films, in contrast to commercially available ITO substrates.[37] For the Rabi measurements, the prepared diamond was transferred to a self-designed printed circuit board (PCB) and contacted with 20 µm copper wire using silver paste. On one side, the PCB was 50 Ω terminated and on the other side a sub miniature version A (SMA) connector was placed.

Simulations

All microwave fields were simulated by using the Comsol Multiphysics RF-module. The measured electrical properties of the ITO layers were used to model the strip line structure in a 2D frequency domain mode analysis. To determine the position of the implanted NV layer, Monte-Carlo simulations using the stopping and range of ions in matter program (SRIM)[24] were done. Since the depth distribution of ions is not symmetrical in the used energy regime, the mean of the depth $\bar{x} = \sum_x xP(x)$ obtained from the probability mass function $P(x)$ was used in the simulations. The depth spread of the NVs can be estimated by analysing the standard deviation $\sigma = \sum_x (x - \bar{x})^2 P(x)$. Ninety percent of all NVs are in a region of $\bar{x} \pm 1.6\sigma$.

Experimental setup

All optical measurements were done on a home-built confocal microscope. A 532 nm laser (LaserQuantum gem532) was used for the excitation and pulsed with an acousto-optic modulator (AA Opto-Electronic). The fluorescence was collected through a ×100 0.95 NA objective and detected with two avalanche photo diodes. Additionally, it was possible to analyse the fluorescence with a spectrometer (Jarrell Ash 82-497 250 mm monochromator with Andor iDus 416 CCD-camera). The microwave was generated with a Ettus USRP B200mini-i and amplified with a Mini Circuits ZHL-16W-43+. All

triggering was managed by a Tectronix AWG520. The static magnetic field was produced by a permanent magnet mounted on a x-z-φ stage.

REFERENCES

1. Casola, F., van der Sar, T. & Yacoby, A. Probing condensed matter physics with magnetometry based on nitrogen-vacancy centres in diamond. *Nat. Rev. Mater.* **3**, 17088 (2018).
2. Dolde, F. et al. Electric-field sensing using single diamond spins. *Nat. Phys.* **7**, 459–463 (2011).
3. Doherty, M. W. et al. Electronic properties and metrology applications of the Diamond NV-center under pressure. *Phys. Rev. Lett.* **112**, 047601 (2014).
4. Wang, J. et al. High-sensitivity temperature sensing using an implanted single nitrogen-vacancy center array in diamond. *Phys. Rev. B* **91**, 155404 (2015).
5. Dutt, M. V. G. et al. Quantum register based on individual electronic and nuclear spin qubits in diamond. *Science* **316**, 1312–1316 (2007).
6. van Oort, E., Manson, N. B. & Glasbeek, M. Optically detected spin coherence of the diamond n-v centre in its triplet ground state. *J. Phys. C: Solid State Phys.* **21**, 4385–4391 (1988).
7. Bourgeois, E. et al. Photoelectric detection of electron spin resonance of nitrogen-vacancy centres in diamond. *Nat. Commun.* **6**, 8577 (2015).
8. Chipaux, M. et al. Magnetic imaging with an ensemble of nitrogen-vacancy centers in diamond. *Eur. Phys. J. D* **69**, 166 (2015).
9. Simpson, D. A. et al. Electron paramagnetic resonance microscopy using spins in diamond under ambient conditions. *Nat. Commun.* **8**, 458 (2017).
10. Sasaki, K. et al. Broadband, large-area microwave antenna for optically detected magnetic resonance of nitrogen-vacancy centers in diamond. *Rev. Sci. Instrum.* **87**, 053904 (2016).

11. Chen, Y. et al. Large-area, tridimensional uniform microwave antenna for quantum sensing based on nitrogen-vacancy centers in diamond. *Appl. Phys. Express* **11**, 123001 (2018).

12. Karsthof, R., von Wenckstern, H. & Grundmann, M. Semitransparent ZnO-based UV-active solar cells: Analysis of electrical loss mechanisms. *J. Vac. Sci. Technol. B* **34**, 04J107 (2016).

13. Zhang, Z., von Wenckstern, H., Lenzner, J., Lorenz, M. & Grundmann, M. Visible-blind and solar-blind ultraviolet photodiodes based on (InxGa1-x)2o3. *Appl. Phys. Lett.* **108**, 123503 (2016).

14. Karsthof, R., von Wenckstern, H. & Grundmann, M. Transparent JFETs based on *p*-NiO/*n*-ZnO heterojunctions. *IEEE Trans. Electron Devices* **62**, 3999–4003 (2015).

15. Yang, C. et al. Room-temperature domain-epitaxy of copper iodide thin films for transparent CuI/ZnO heterojunctions with high rectification ratios larger than 10^9. *Sci. Rep.* **6**, 21937 (2016).

16. Pluk, H., Stokes, D., Lich, B., Wieringa, B. & Fransen, J. Advantages of indium-tin oxide-coated glass slides in correlative scanning electron microscopy applications of uncoated cultured cells. *J. Microsc.* **233**, 0022–2720 (2009).

17. Nakahata, H. et al. Diamond-based surface acoustic wave devices. *Semicond. Sci. Technol.* **18**, S96–S104 (2003).

18. Wisz, G., Virt, I., Sagan, P., Potera, P. & Yavorskyi, R. Structural, optical and electrical properties of zinc oxide layers produced by pulsed laser deposition method. *Nanoscale Res. Lett.* **12**, 253 (2017).

19. Hachigo, A., Nakahata, H., Higaki, K. & Fujii, S. Heteroepitaxial growth of ZnO films on diamond (111) plane by magnetron sputtering. *Appl. Phys. Lett.* **65**, 2556–2558 (1994).

20. Mora-Fonz, D. & Shluger, A. L. Making amorphous ZnO: Theoretical predictions of its structure and stability. *Phys. Rev. B* **99**, 014202 (2019).

21. Xiao, Y. et al. Amorphous indium tin oxide films deposited on flexible substrates by facing target sputtering at room temperature. *Thin Solid Films* **556**, 155–159 (2014).

22. Appel, P., Ganzhorn, M., Neu, E. & Maletinsky, P. Nanoscale microwave imaging with a single electron spin in diamond. *New J. Phys.* **17**, 112001 (2015).

23. Horsley, A. et al. Microwave device characterization using a widefield diamond microscope. *Phys. Rev. Appl.* **10**, 044039 (2018).

24. Ziegler, J. F., Ziegler, M. & Biersack, J. SRIM – the stopping and range of ions in matter (2010). *Nucl. Instrum. Methods in Phys. Res. B* **268**, 1818–1823 (2010).

25. van der Pauw, L. J. A method of measuring specific resistivity and hall effect of discs of arbitrary shape. *Philips Res. Rep.* **13**, 1–9 (1958).

26. Element six technologies. US Corporation 3901 Burton Drive, Santa Clara, CA.

27. Zheng, J. & Kwok, H. Preparation of indium tin oxide films at room temperature by pulsed laser deposition. *Thin Solid Films* **232**, 99–104 (1993).

28. Balasubramanian, N. & Subrahmanyam, A. Electrical and optical properties of reactively evaporated indium tin oxide (ITO) films-dependence on substrate temperature and tin concentration. *J. Phys. D: Appl. Phys.* **22**, 206–209 (1989).

29. Comsol multiphysics v. 5.2a. www.comsol.com. COMSOL AB, Stockholm, Sweden.

30. Michl, J. et al. Perfect alignment and preferential orientation of nitrogen-vacancy centers during chemical vapor deposition diamond growth on (111) surfaces. *Appl. Phys. Lett.* **104**, 102407 (2014).

31. Lesik, M. et al. Perfect preferential orientation of nitrogen-vacancy defects in a synthetic diamond sample. *Appl. Phys. Lett.* **104**, 113107 (2014).

32. Gobbi, P. et al. Correlative high-resolution morphologic analysis of the three-dimensional organization of human chromosomes. *Scanning* **22**, 273–281 (2006).

33. Guo, M. et al. Monitoring of cell growth and assessment of cytotoxicity using electrochemical impedance spectroscopy. *Biochimica et Biophysica Acta (BBA) - General Subjects* **1760**, 432–439 (2006).

34. Nashimoto, Y. et al. Measurement of gene expression from single adherent cells and spheroids collected using fast electrical lysis. *Anal. Chem.* **79**, 6823–6830 (2007).

35. Petronis, S., Stangegaard, M., Christensen, C. B. & Dufva, M. Transparent polymeric cell culture chip with integrated temperature control and uniform media perfusion. *BioTechniques* **40**, 368–376 (2006).

36. Rushe, N. et al. Cytocompatibility of novel tin oxide thin films. *J. Mater. Sci.: Mater. Med.* **16**, 247–252 (2005).

37. Majumdar, H. S., Majumdar, S., Tobjörk, D. & Österbacka, R. Ferromagnetism in indium tin-oxide (ITO) electrodes at room temperature. *Synth. Met.* **160**, 303–306 (2010).

AUTHOR CONTRIBUTIONS

R.S. and R.J. performed the Rabi and transmission measurements. The data analysis, simulations/calculations were done by R.S. The ITO layers were deposited by M.K. The paper was written by R.S. with feedback from all authors.

COMPETING INTERESTS

The authors declare no competing interests.

ADDITIONAL INFORMATION

Supplementary information is available for this paper at https://doi.org/10.1038/s41534-019-0216-1.

Correspondence and requests for materials should be addressed to R.S.

Reprints and permission information is available at http://www.nature.com/reprints

Publisher's note Springer Nature remains neutral with regard to jurisdictional claims in published maps and institutional affiliations.